X-ray Photoemission Electron Microscopy, a tool for the investigation of complex magnetic structures

Andreas Scholl,[1] Hendrik Ohldag,[2] Frithjof Nolting,[3] Joachim Stöhr,[2] Howard A. Padmore[1]

[1] Lawrence Berkeley National Laboratory, 1 Cyclotron Road, Berkeley, CA 94720
[2] Stanford Synchrotron Radiation Laboratory, PO Box 20450, Stanford, CA 94309
[3] Swiss Light Source, Paul Scherrer Institute, CH 5232 Villigen PSI, Switzerland

Abstract

X-ray Photoemission Electron Microscopy unites the chemical specificity and magnetic sensitivity of soft x-ray absorption techniques with the high spatial resolution of electron microscopy. The discussed instrument possesses a spatial resolution of better than 50 nm and is located at a bending magnet beamline at the Advanced Light Source, providing linearly and circularly polarized radiation between 250 and 1300 eV. We will present examples which demonstrate the power of this technique applied to problems in the field of thin film magnetism. The chemical and elemental specificity is of particular importance for the study of magnetic exchange coupling because it allows separating the signal of the different layers and interfaces in complex multi-layered structures.

Introduction

The development of x-ray magnetic dichroism techniques has led to a significant improvement in our understanding of the physics of magnetic materials. The tunability of the x-ray energy and the availability of polarized (linear, circular) radiation at modern synchrotron sources facilitates the investigation of complex, multi-element, magnetic structures utilizing the element specificity of x-ray techniques to separate the contribution of different layers and elements to the magnetism of a system [1]. X-ray magnetic dichroism using polarized radiation gives quantitative access to the magnetization of the sample [2]. X-ray spectromicroscopy techniques such as Photoemission Electron Microscopy (PEEM) or Transmission X-Ray Microscopy (TXM) add spatial resolution for the investigation of structured or laterally inhomogeneous systems [3,4]. In this paper we will give an overview over the PEEM technique and discuss the data acquisition and data analysis using the ferromagnet/antiferromagnet bi-layer system Co/$LaFeO_3$ as an example. The magnetic structure of $LaFeO_3$ grown on $SrTiO_3$(001) has been discussed in detail in [5] and is closely related to the perovskite structure of the $LaFeO_3$ layer. The coupling at the Co/$LaFeO_3$ interface has been described in [6]. Similar measurements using PEEM were also carried out on Co/NiO(001) [7-9]. The sample is a Co/$LaFeO_3$ double wedge with a Co thickness between 0.4 and 2 nm and a $LaFeO_3$ thickness between 4 and 20 nm. The films were grown on a $SrTiO_3$(001) singe crystal substrate with a 2° miscut which causes preferential growth of one class of domains which have in-plane projections of the magnetic axis along the c-axis of $LaFeO_3$ [10].

Experimental setup

The PEEM-2 is a full-field imaging photoemission microscope using a 4-lens optics, see Fig. 1. Electrostatic lenses are used for focusing and projection to prevent any external influence on the sample magnetization. A detailed description of the instrument can be found in [3]. The microscope images secondary electrons emitted from the sample upon illumination with x rays. The electrons are accelerated by a strong electric field (~20 kV) between sample and the objective lens of the microscope. The electrons are detected after a magnification by a factor of 1000-2000 on a phosphor screen which is read by a slow scan CD detector. An aperture in the back focal plane of the second lens (transfer lens) is used to limit the angular and energy acceptance of the microscope reducing the spherical and chromatic aberrations of the electron optics. Using a 12 mm pin hole the best spatial resolution of the microscope of well below 50 nm at a transmission of about 3% was reached, close to the design resolution of 20 nm. The typical spatial resolution for magnetic imaging is between 50 and 100 nm because of the relatively small magnetic image contrast. Deflector and stigmator elements located in the back focal plane of the objective lens and the first projection lens are used to correct for small mechanical misalignments of the microscope. The local image intensity at the detector is approximately given by $I \sim I_0\mu(E)$. I_0 is the x-ray flux and μ is the local absorption coefficient of the imaged sample area at the x-ray energy E, neglecting saturation effects which, however, become significant on strong absorption resonances [10]. The image intensity is furthermore modulated by the local work function of the sample, especially in threshold excitation using UV light, and the sample topography which causes micro-focusing of the emitted electrons. The probing depth in metals and oxides is typically about 2 nm [11]. Contrast in PEEM images is therefore a superposition of absorption, work function and topographic contrast. We can discriminate between these different contrasts by variation of the photon energy because only absorption contrast is energy dependent if x-rays are used. By tuning the photon energy to an absorption edge elemental and chemical specificity is achieved utilizing the characteristic near edge fine structure of atoms in different chemical environments. The instrument is located at beamline 7.3.1.1 of the Advanced Light Source which provides bending magnetic radiation between 250-1300 eV. A moveable aperture in the beamline is used to change the photon polarization from linear to left and right circular. The photon incidence angle is 30° with the linear polarization vector **E** parallel to the sample plane. The energy resolution of the beamline, which is optimized for high flux, is between $E/\Delta E \approx 1000$-1800.

Magnetic x-ray dichroism

Using x-ray magnetic dichroism PEEM is sensitive to the magnetic domain structure of magnetically ordered materials. In 3d transition metals dichroism is strongest at the L resonances ($2p \rightarrow 3d$). X-ray Magnetic Circular Dichroism (XMCD) using circularly polarized x-rays probes the angle φ between the sample magnetization direction **M** and the photon spin s, which is aligned with the photon propagation direction. It has opposite sign at the L_3 and the L_2 edge and changes sign when either the magnetization direction or the photon helicity are reversed. Its angular dependence is given by:

$$I_{XMCD} \sim |M| \cos\varphi(\mathbf{M},\mathbf{s}) . \quad (1)$$

Contrast in PEEM images results from the variation in angle φ between the x-ray polarization and the magnetization of different domains [4]. X-ray Magnetic Linear Dichroism (XMLD) using linearly polarized x-rays probes the anisotropy of the sample, which either originates from structure or magnetism. Strong magnetic linear dichroism contrast has been observed by spectroscopy in NiO, Fe_2O_3, and $LaFeO_3$ [10,12,13] and by microscopy in NiO and $LaFeO_3$ [5-9]. The effect appears at multiplet peaks at the L_3 and the L_2 edges of the oxides, as shown in the Fig. 2. The two local spectra were acquired from magnetic domains with different orientation of the antiferromagnetic axis using PEEM. The XMLD effect changes sign at different multiplet peaks of the same edge (peak A versus B) but has a similar structure at the L_3 and L_2 edges. Its angular dependence is given by:

$$I_{XMLD} \sim |M^2|(3-\cos^2\varphi(\mathbf{A},\mathbf{E})) . \quad (2)$$

φ is the angle between the antiferromagnetic axis **A** and the linear polarization vector **E**. In $LaFeO_3$ a stronger 2nd peak at the L_3 and the L_2 edge is characteristic for a preferentially parallel orientation of **A** and **E** [5]. Therefore the magnetization axis in domain 2 is closer to the linear x-ray polarization vector than in domain 1. Antiferromagnets usually do not show circular dichroism because the magnetic structure is completely compensated. Magnetic linear dichroism contrast can be distinguished from structural contrast using the characteristic temperature dependence of the magnetic contrast which vanishes above the ordering temperature of the temperature (Néel temperature).

Image acquisition and analysis

A PEEM image I_t acquired using an exposure time t needs to be corrected for the spatially varying dark count rate and sensitivity of the PEEM detector system. This is achieved by subtraction of a dark image D_t and division by a sensitivity image $S_{t'}$: $I = (I_t - D_t)/S_{t'}$. The dark image D_t is acquired without x-ray illumination using the same exposure time t. Imaging a sample with a totally defocused microscope and subtracting the dark image generates the sensitivity image $S_{t'}$. The exposure time t' of the sensitivity image differs from t because the detector sensitivity variation is not directly a function of the exposure time but of the electron flux per time which reaches the detector. Experimentally a t' fulfilling $t' = t\frac{\overline{S_{t'}}}{\overline{I_t}}$ has produced good results. $\overline{S_{t'}}$ and $\overline{I_t}$ are the spatially averaged intensities of the sensitivity and the acquired PEEM image. Usually we adjust the electron flux during acquisition of the sensitivity image such that the CCD is half filled in t'. If the image intensity is high and the exposure time short then subtraction of the dark image can be omitted. Dark and sensitivity images can be reused and only have to measured once because the detector sensitivity is constant in time. Fig. 3 a,b) demonstrates the improvement of the image quality showing images before a) and after the correction b) for a exposure time of 70 s.

To generate magnetic domain images we take advantage of the change in sign of the linear and circular dichroism signal in the near edge spectrum. The procedure is

illustrated in Fig. 3 b-f). Images b) and c) were acquired on a Co/$LaFeO_3$ film at the b) Co L_3 and c) L_2 edge and are both sensitivity corrected. They both show the same ferromagnetic Co domain pattern but with opposite contrast. The magnetic contrast can be enhanced and non-magnetic contrast suppressed by calculating d) difference (L_3-L_2), e) ratio (L_3/L_2), and f) asymmetry ([L_3-L_2]/[L_3+L_2]) images. The ratio and asymmetry image are normalized to the image intensity and therefore correct an inhomogeneous sample illumination. The asymmetry image is especially useful in a quantitative analysis because the intensity difference between different domains is a measure for the relative angle between the magnetization in both domains. If the dichroism is weak compared to the total image intensity then the ratio image is equivalent to the asymmetry image. In the following we will always use ratio images which on a ferromagnet are called *XMCD images* (L_3/L_2) and on an antiferromagnet are called *XMLD images* (L_3B/L_3A). L_3A and L_3B are the two prominent multiplet peaks at the L_3 edge (Fig. 2). Antiferromagnetic domains with a more parallel orientation of the magnetic axis relative to the linear x-ray polarization vector appear brighter in the XMLD image. Ferromagnetic domains with a parallel orientation of the magnetization direction relative to the circular x-ray polarization vector appear brighter in the XMCD image than domains with an antiparallel orientation.

Domain correlation

The moderate surface sensitivity of PEEM using secondary electrons as a probe permits the study of layered samples. We furthermore use the elemental specificity of X-ray PEEM to separate the signal from different magnetic layers. This procedure is demonstrated in Fig. 4. We have studied an approximately 1.2 nm thick ferromagnetic Co film grown on an 8 nm thick antiferromagnetic $LaFeO_3$ film. Shown from top to bottom are a,b) XMCD images of the ferromagnetic structure of the Co layer on top of $LaFeO_3$, c,d) XMCD images showing a ferromagnetic polarization of the antiferromagnetic $LaFeO_3$ layer in contact with the ferromagnetic Co, and e,f) XMLD images of the antiferromagnetic domain structure of the $LaFeO_3$ layer acquired at the Fe L_3 edge. The images were acquired in two geometries which differ by an azimuthal rotation of the sample of 90°. The images were rotated back by software to show identical image areas. The direction of incidence of the x-ray beam is shown above the images. The Fe XMLD images show a reversal in contrast after the azimuthal rotation by 90°, demonstrating the 180° periodicity of the linear dichroism signal. The XMCD signal – on the other hand – has 360° periodicity, explaining the vanishing contrast in the upper half of the image after the 90° azimuthal rotation. Arrows illustrate the direction of the magnetization in the ferromagnet and the in-plane orientation of the antiferromagnetic axis as derived from the evolution of the image contrast while rotating the sample. The upper half of the imaged sample area has a preferentially horizontal orientation of the magnetic axis, causing the brighter intensity of this area in f), whereas the lower half has a vertical orientation. Prior measurements have shown that the antiferromagnetic axis is canted by 45° from the surface, which means that the XMLD contrast is actually due to the variation of the in-plane projection of the magnetic axis [5,10]. Apparently the magnetization of the ferromagnet and the in-plane projection of the antiferromagnet spin axis are always aligned parallel indicating a uniaxial interface exchange coupling of the antiferromagnet and the ferromagnet. The high sensitivity of PEEM to weak magnetic signals furthermore

allows imaging the ferromagnetic polarization of antiferromagnetic $LaFeO_3$ in contact with the ferromagnet Co. The Fe XMCD signal shows the same domain pattern as the Co layer, revealing a ferromagnetic coupling of the uncompensated fraction of the $LaFeO_3$ layer to Co. The origin of the polarization can either be a ferromagnetically ordered $LaFeO_x$ interface layer, as was observed at the NiO/Co interface [14,15], or a ferromagnetic polarization of the whole $LaFeO_3$ layer. The latter could be promoted by the small thickness of the film, reducing its total anisotropy, and making a polarization by exchange coupling to the adjacent ferromagnet more effective. Note that $LaFeO_3$ has a weak parasitic ferromagnetic moment that could be ordered parallel to the magnetization of the Co by the strong interface exchange coupling [16].

Magnetization maps

The information from Fig. 4 e,f) can be used to generate maps of the direction and the size of the local sample magnetization. This is demonstrated in Fig. 5 for Co. According to (1) the XMCD signal in 4 e) and 4 f) is given by

$I^{e}_{XMCD} = I_0 + \alpha|M|\cos(90° - \varphi) = I_0 + \alpha|M|\sin(\varphi)$ and $I^{f}_{XMCD} \sim I_0 + \alpha|M|\cos(\varphi)$,

respectively, with φ denoting the angle between the magnetization **M** and **x,** and $|M|$ the value of the in-plane projection of the magnetization. The non-magnetic image intensity I_0 is approximately equal to the average intensity of the XMCD image because domains pointing up, down, left, and right appear about equally often. α is a scaling factor. Inverting these equations pixel-by-pixel produces the magnetization maps in Fig. 5. The value of the magnetization shown on the left is approximately constant over the image, except for the domain wall regions. The reduced signal near the walls can be explained by a domain wall thickness below the experimental resolution. This resolution consists of the microscope resolution and errors in the alignment of the rotated XMCD images. From the width of the lines we determine an upper limit for the wall width of 80-100 nm. The spatial distribution of the magnetization direction is shown on the right. The relation between gray levels and angles is explained in the “color”-wheel. 4 gray levels: black, lightgray, darkgray, white, correspond to 4 directions up, down, left, right. A similar procedure can be used to generate magnetization maps of antiferromagnets with the difference that images after an azimuthal rotation of 45° are required because of the 180° periodicity of XMLD.

Thickness dependent contrast

Fig. 6 shows the dependence of the domain contrast as function of the thickness of the ferromagnetic Co layer, measured on a Co wedge between 0.8 – 1.6 nm grown on 1.2 nm $LaFeO_3$. The top row shows the Co domain images acquired with XMCD, the center row shows XMCD images of the ferromagnetic moment of the $LaFeO_3$ layer and the bottom row shows XMLD images of the antiferromagnetic structure of the $LaFeO_3$ layer. The $LaFeO_3$ layer is mostly single domain with an in-plane projection of the magnetization axis along the vertical. A number of very small domains, close in size to the spatial resolution of the microscope are horizontally aligned. They are responsible for the lighter speckles in the XMLD images. The XMCD images show two levels of brightness belonging to domains with magnetization in the up and the down direction, aligned with the in-plane projection of the $LaFeO_3$ magnetic axis. The Co magnetization shows a

reduction in contrast for decreasing film thickness which is explained by the smaller Co peak intensity in a thinner film. Very thin Co films (≈0.8 nm) become non-magnetic. Interestingly we observe the same Co thickness dependence of the domain contrast in the $LaFeO_3$ layer. The contrast vanishes with decreasing Co thickness and finally disappears together with the Co magnetic signal. This observation suggests that the detected uncompensated Fe moment is indeed due to a polarization effect caused by the strong interface exchange coupling at the ferromagnet/antiferromagnet boundary.

Conclusion

We have demonstrated some of the abilities of Photoemission Electron Microscopy, making this technique an ideal tool for the investigation of laterally structured, phase separated or inhomogeneous surfaces and thin films. Polarized radiation from a 3rd generation synchrotron source allows the study of ferromagnetically and antiferromagnetically ordered magnetic systems with high spatial resolution and sub-monolayer sensitivity. Sensitivity, spatial resolution and also the time resolution for the investigation of dynamic processes can be improved by using an aberration free electron optics. The spherical and also partly the chromatic aberrations of the microscope can be compensated by using an electron mirror which is designed to have exactly the opposite aberrations, which then cancel out on the detector. Two groups, the SMART collaboration at BESSY 2 [17] and the PEEM-3 collaboration at the Advanced Light Source [18] currently design and build aberration corrected microscopes which are aiming at a spatial resolution of a few nm. The second advantage of aberration correction is the much improved microscope transmission at an intermediate spatial resolution of a few 10 nm because energy filtering either by an imaging energy analyzer or an aperture in a dispersive plane will be unnecessary increasing the transmission of the microscope by at least one order of magnitude. Together with a tighter focusing of the synchrotron beam an increase in sensitivity by at least a factor of 30 and an increase in the speed of image acquisition by a factor of 1000 will be possible. Dynamics in the ms regime will be directly accessible. A different approach to measure dynamics is by stroboscopic pump-probe techniques. A synchronized laser – x-ray PEEM experiment utilizing the pulsed time structure of the synchrotron source is currently set up at the Advanced Light Source. This experiment will give access to the important ps-ns regime, the typical time scale of magnetization precession and magnetization damping. Compared to traditional optical techniques PEEM offers the advantages of a much higher spatial resolution, higher sensitivity, and elemental specificity.

Acknowledgements

The $LaFeO_3$ sample preparation and characterization was carried out at the IBM research centers in Almaden, USA and Zürich, Switzerland. The authors thank M. Jin Won Seo, J.-P. Locquet, J. Fompeyrine, H. Siegwart, E. Fullerton, M.F. Toney, J. Lüning, and S. Anders who contributed to this work. This work was supported by the Director, Office of Basic Energy Sciences, of the US Department of Energy.

Figures

Fig. 1: Experimental setup (schematic) of the PEEM-2 microscope.

Fig. 2: Local PEEM absorption spectra acquired in two antiferromagnetic domains on $LaFeO_3$. The linear dichroism at the L_3 and the L_2 edge results from a different orientation of the antiferromagnetic axis in these domains relative to the linear x-ray polarization.

Fig. 3: PEEM images acquired at the Co L edges: a) L_3 edge, as acquired, b) L_3 edge after noise compensation, c) L_2 edge after noise compensation. d) difference image, e) ratio image, f) asymmetry image. Images d-f) show the ferromagnetic domain structure of the Co layer with enhanced contrast

Fig. 4: XMCD images of a,b) the Co layer, c,d) the $LaFeO_3$ layer acquired at the Fe edge showing the ferromagnetic domain structure, and e,f) XMLD images of the $LaFeO_3$ layer showing the antiferromagnetic domain structure. Arrows mark the spin direction. The images were acquired in two geometries, rotated by 90° around the surface normal.

Fig. 5: Maps showing the size and the direction of the magnetization in the Co layer averaged over the spatial resolution of the microscope.

Fig. 6: Thickness dependence of the ferromagnetic domain contrast in the Co layer (top row) and the $LaFeO_3$ layer (center row). Thickness dependence of the antiferromagnetic domain contrast in the $LaFeO_3$ layer (bottom row).

References

[1] J.B. Kortright, D.D. Awschalom, J. Stöhr, S.D. Bader, Y.U. Idzerda, S.S.P. Parkin, I.K. Schuller, and H.C. Siegmann, J. Magn. Magn. Mater. **207**, 7 (1999).

[2] C. T. Chen, F. Sette, Y. Ma, and S. Modesti, Phys. Rev. B **42**, 7262 (1990).

[3] S. Anders, H. A. Padmore, R. M. Duarte, T. Renner, Th. Stammler, A. Scholl, M. R. Scheinfein, J. Stöhr, L. Séve, and B. Sinkovic, Rev. Sci. Instrum. **70**, 3973 (1999).

[4] J. Stöhr, Y. Wu, B.D. Hermsmeier, M.G. Samant, G.R. Harp, S. Koranda, D. Dunham, and B.P. Tonner, Science **259**, 658 (1993).

[5] A. Scholl, J. Stöhr, J. Lüning, J.W. Seo, J. Fompeyrine, H. Siegwart, J.-P. Locquet, F. Nolting, S. Anders, E.E Fullerton, M.R. Scheinfein, and H.A. Padmore, Science **287**, 1014 (2000).

[6] F. Nolting, A. Scholl, J. Stöhr, J.W. Seo, J. Fompeyrine, H. Siegwart, J.-P. Locquet, S. Anders, J. Lüning, E.E. Fullerton, M.F. Toney, M.R. Scheinfein, and H.A. Padmore, Nature **405**, 767 (2000).

[7] J. Stöhr, A. Scholl, T.J. Regan, S. Anders, J. Lüning, M.R. Scheinfein, H.A. Padmore, and R.L. White, Phys. Rev. Lett. **83,** 1862 (1999).

[8] F.U. Hillebrecht, H. Ohlag, N.B. Weber, C. Bethke, U. Mick, M. Weiss, and J. Bahrdt, Phys. Rev. Lett. **86**, 3419 (2001).

[9] H. Ohldag, A. Scholl, F. Nolting, S. Anders, F.U. Hillebrecht, and J. Stöhr, Phys. Rev. Lett. **86**, 2878 (2001).

[10] J. Lüning, F. Nolting, H. Ohldag, A. Scholl, E.E. Fullerton, M. Toney, J.W. Seo, J. Fompeyrine, H. Siegwart, J.-P. Locquet, J. Stöhr, submitted to Phys. Rev. B (2001)

[11] R. Nakajima, J. Stöhr, and Y. U. Idzerda, Phys. Rev. B **59**, 6421 (1999).

[12] D. Alders, L.H. Tjeng, F.C. Voogt, T. Hibma, G.A. Sawatzky, C.T. Chen, J. Vogel, M. Sacchi, and S. Iacobucci, Phys. Rev. B **57**, 11623(1998).

[13] P. Kuiper, B.G. Searle, P.Rudolf, L.H.Tjeng, andC.T. Chen, Phys. Rev. Lett.**70**, 1549 (1993).

[14] T. J. Regan, H. Ohldag, C. Stamm, F. Nolting, J. Lüning,, J. Stöhr, and R. L. White, Phys. Rev. B (in press) (2001)

[15] H. Ohldag, T.J. Regan, J. Stöhr, A. Scholl, F. Nolting, J. Lüning, C. Stamm, S. Anders, and R.L. White, submitted to Phys. Rev. Lett. (2001)

[16] M. Eibschütz, S. Shtrikman, D.Treves, Phys. Rev. **156**, 562 (1967).

[17] R. Fink, M.R. Weiss, E. Umbach, D. Preikszas, H. Rose, R. Spehr, P. Hartel, W. Engel, R. Degenhardt, R. Wichtendahl, H. Kuhlenbeck, W. Erlebach, K. Ihmann, R. Schlogl, H.J. Freund, A.M. Bradshaw, G. Lilienkamp, T. Schmidt, E. Bauer, G. Benner, J. Electron Spectrosc. Relat. Phenom. **84**, 231 (1997).

[18] J. Feng, H. Padmore, D. H. Wei, S. Anders, Y.Wu, A.Scholl and D.Robin, Proceeding of the SRI2001, submitted to Rev. Sci. Instrum (2001).

Fig. 1

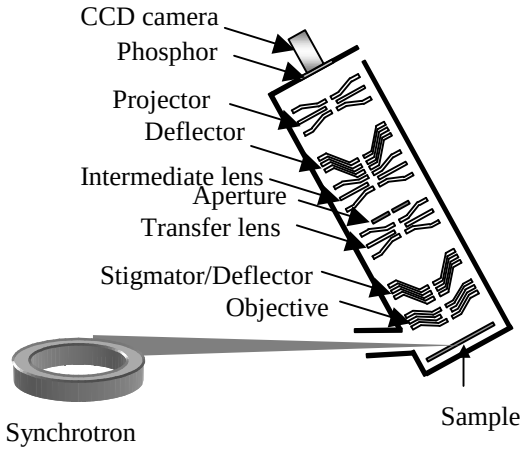
CCD camera
Phosphor
Projector
Deflector
Intermediate lens
Aperture
Transfer lens
Stigmator/Deflector
Objective
Synchrotron
Sample

Fig. 2

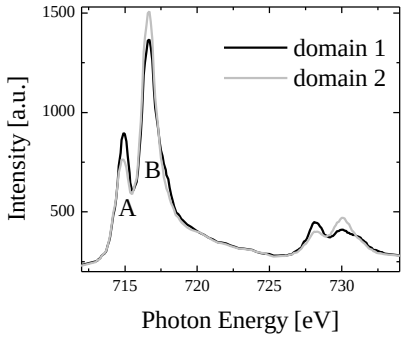
1500
1000
500
Intensity [a.u.]
domain 1
domain 2
A
B
715
720
725
730
Photon Energy [eV]

Fig. 3

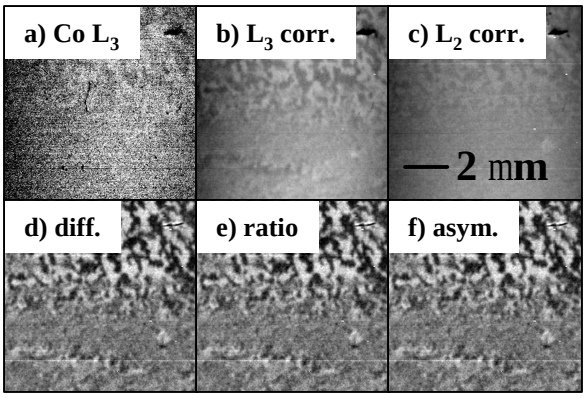

Fig. 4

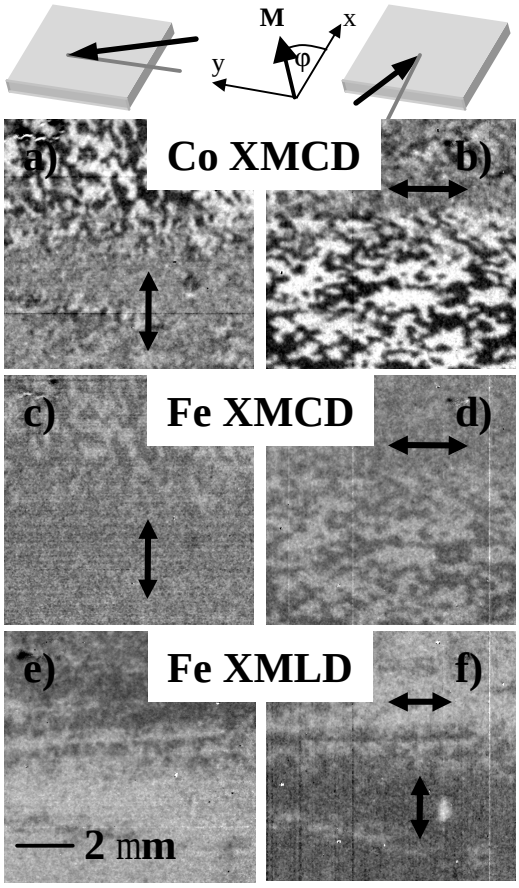

Fig. 5

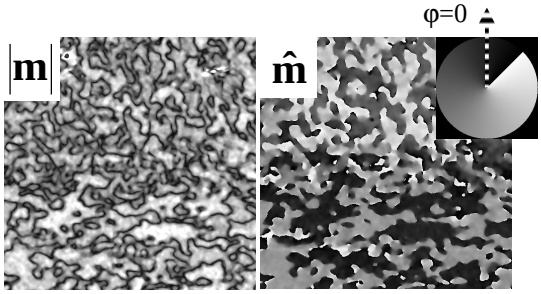
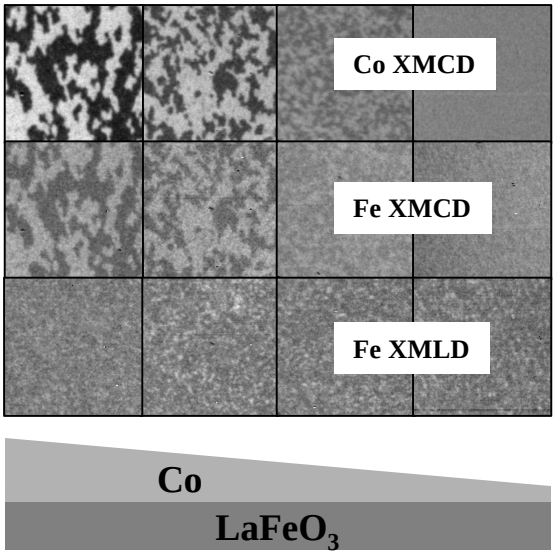
Fig. 6